Journal of
Materials Chemistry A

Accepted Manuscript

This article can be cited before page numbers have been issued, to do this please use: J. Puszkiel, M. V. Castro Riglos, J. M. Ramallo-López, M. Mizrahi, F. Karimi, A. Santoru, A. Hoell, F. C. Gennari, P. Arneodo Larrochette, C. Pistidda, T. Klassen, J. M. Bellosta von Colbe and M. Dornheim, *J. Mater. Chem. A*, 2017, DOI: 10.1039/C7TA03117C.

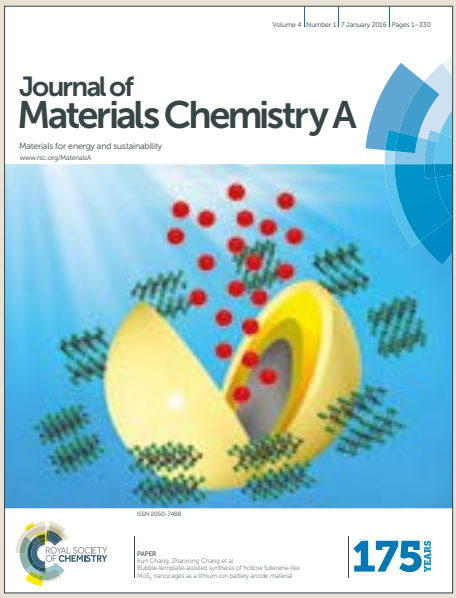

ROYAL SOCIETY OF CHEMISTRY

rsc.li/materials-a

ROYAL SOCIETY OF CHEMISTRY View Article Online
DOI: 10.1039/C7TA03117C

Journal Name

ARTICLE

Novel catalytic route for hydrogenation-dehydrogenation of 2LiH+MgB_2 *via in-situ* formed core-shell Li_xTiO_2 nanoparticles†

liReceived 00th January 20xx,
Accepted 00th January 20xx

DOI: 10.1039/x0xx00000x

www.rsc.org/

J.A. Puszkiel,*[a,d] M.V. Castro Riglos,[b] J.M. Ramallo-López,[c] M. Mizrahi,[c] F. Karimi,[d] A. Santoru,[d] A. Hoell,[e] F.C. Gennari,[a] P. Arneodo Larochette,[a] C. Pistidda,[d] T. Klassen,[d,f] J.M. Bellosta von Colbe[d] and M. Dornheim[d]

Aiming to improve the hydrogen storage properties of 2LiH+MgB_2 (Li-RHC), the effect of TiO_2 addition to Li-RHC is investigated. The presence of TiO_2 leads to the *in-situ* formation of core-shell Li_xTiO_2 nanoparticles during milling and upon heating. These nanoparticles markedly enhance the hydrogen storage properties of Li-RHC. Throughout hydrogenation-dehydrogenation cycling at 400 °C a 1 mol % TiO_2 doped Li-RHC material shows sustainable hydrogen capacity of ~ 10 wt.% and short hydrogenation and dehydrogenation times of just 25 and 50 minutes, respectively. The *in-situ* formed core-shell Li_xTiO_2 nanoparticles confer proper microstructural refinement to the Li-RHC thus preventing the material's agglomeration upon cycling. An analysis of the kinetic mechanisms shows that the presence of the core-shell Li_xTiO_2 nanoparticles accelerates the one dimensional interface-controlled mechanism during hydrogenation owing to the high Li^+ mobility through the Li_xTiO_2 lattice. Upon dehydrogenation, the *in-situ* formed core-shell Li_xTiO_2 nanoparticles do not modify the dehydrogenation thermodynamic properties of the Li-RHC itself. A new approach by the combination of two kinetic models evidences that the activation energy of both MgH_2 decomposition and MgB_2 formation are reduced. These improvements are due to a novel catalytic mechanism *via* Li^+ source/sink reversible reactions.

Introduction

One of the main constraints for the practical application of hydrogen is the lack of an efficient and safe hydrogen storage system. Hydrogen storage through hydride compounds formation is a potential alternative to address this problem[1]. Lithium reactive hydride composite (Li-RHC), i.e. 2LiH+MgB_2 or 2$LiBH_4$+MgH_2 stoichiometric hydride mixture, presents potential characteristics as hydrogen storage medium for practical applications. According to the reaction $2LiBH_{4(s)} + MgH_{2(s)} \leftrightarrows 2LiH_{(s)} + MgB_{2(s)} + 4H_{2(g)}$, Li-RHC has suitable theoretical reaction enthalpy of 46 kJ/mol H_2 at standard conditions due to the exothermic formation of MgB_2 upon H_2 release and theoretical weight hydrogen capacity of 11.4 wt.%[2]. Vajo *et. al.*[3] have reported the experimental thermodynamic parameters of the Li-RHC+1–3 mol % $TiCl_3$ based on the hydrogenation equilibrium pressures (re-hydrogenation reaction): ΔH_{uptake}= 40.5 kJ/mol H_2, ΔS_{uptake}= 81.3 J/K mol H_2 and reversible storage of 8–10 wt % of hydrogen. Jepsen *et. al.*[4] have shown experimental and reversible gravimetric hydrogen storage capacity of about 9 wt % H for loose and compacted Li-RHC+5 mol % $TiCl_3$. In addition, Li-RHC works at milder pressure and temperature conditions during the storage process than the conventional methods, i.e. compressed and cryogenic hydrogen storage[5]. Despite all the beneficial characteristics of the Li-RHC, one of the main drawbacks is its slow kinetic behavior. The dehydrogenation under dynamic conditions proceeds in two steps according to the reaction: $2LiBH_{4(l)} + MgH_{2(s)} \rightarrow Mg_{(s)} + 2LiBH_{4(l)} + H_{2(g)} \rightarrow 2LiH_{(s)} + MgB_{2(s)} + 4H_{2(g)}$[6]. On one hand, the first step of the reaction involving the decomposition of MgH_2 is quite fast. On the other hand, the decomposition of $LiBH_4$ and subsequent formation of MgB_2 has sluggish kinetic behavior. This hydride system also reacts throughout different pathways depending on the temperature and pressure conditions and requires an appropriate hydrogen overpressure during the dynamic dehydrogenation process to assure reversible hydrogen uptake-release[7,8]. Another constraint is the poor cycling stability in terms of hydrogen capacity and kinetic behavior[4]. A noticeable improvement in the kinetic behavior of Li-RHC has been observed by the

[a] Department of Physicochemistry of Materials, Consejo Nacional de Investigaciones Científicas y Técnicas (CONICET) and Centro Atómico Bariloche, Av. Bustillo km 9500 S.C. de Bariloche, Argentina. *E-mail: julianpuszkiel1979@gmail.com; Tel: +54 0294 445100 (5556)
[b] Department of Metalphysics, Consejo Nacional de Investigaciones Científicas y Técnicas (CONICET) and Centro Atómico Bariloche, Av. Bustillo km 9500 S.C. de Bariloche, Argentina.
[c] Instituto de Investigaciones Fisicoquímicas Teóricas y Aplicadas, INIFTA (CCT La Plata – CONICET, UNLP), Diagonal 113 y Calle 64, La Plata, Argentina.
[d] Department of Nanotechnology, Institute of Materials Research, Helmholtz–Zentrum Geesthacht, Max-Planck-Straße 1, 21502 Geesthacht, Germany.
[e] Institute for Nanospectroscopy, Helmholtz-Zentrum Berlin, Hahn-Meitner-Platz 1, 14109 Berlin, Germany.
[f] Helmut Schmidt University, Holstenhofweg 85, 22043 Hamburg, Germany.
†Electronic Supplementary Information (ESI) available: See DOI: 10.1039/x0xx00000x

View Article Online
DOI: 10.1039/C7TA03117C

addition of transition metals and transition metal compounds (TM-compounds) *via* the formation of transition metal borides (TM-borides)[9-15], the addition of synthesized nanosized TM-borides[16-19] and nanoconfinement of doped Li-RHC[20-25], nanoscaling or wrapping in graphene nanostructures $MgH_2/LiBH_4$[26-31]. The addition of TM-compounds which leads to the formation of TM–borides appears to provide heterogeneous nucleation sites for the formation of MgB_2 upon desorption[9]. However, TM-compounds such as halides generate by-products, reducing the hydrogen capacity. In addition, the size and dispersion of the TM-borides is not always effective. For this reason the synthesis of nanosized TM-borides has been applied[16-19]. This approach requires the synthesis of TM-boride nanoparticles through several step procedures to avoid by-products and to have an efficient additive dispersion. The nanoconfinement, nanoscaling and wrapped-graphene approaches further improve the kinetic behavior and cycling stability of the Li-RCH compared with the bulk material. Nonetheless, the complexity and mainly the cost of these approaches may pose a major constraint for large scale applications.

Considering the interesting hydrogen storage properties of Li-RHC and the feasibility for a large scale application, herein several experimental advanced techniques are used to shed light onto the beneficial underlying effect of TiO_2 upon the Li-RHC and to assess the hydrogen storage properties of technological interest that this multi-component hydride system has.

Experimental

Materials and preparation

2LiH + MgB_2 reactive hydride composite plus TiO_2 additive was prepared by mechanical milling (MM) in argon atmosphere using a P6 Fritsch Pulverisette planetary device, an 80 cm^3 milling chamber and a ball to powder ratio of 40:1. Mixtures of 2LiH + MgB_2 and different amounts of TiO_2 additive (1 and 5 mol %) were milled for a short time of 2 h in order to minimize the Fe contamination[10]. After the preparation and heating processes for the 2LiH + MgB_2 + TiO_2, the presence of H_2 gas was verified with a Bacharach combustible gas leak detector. As starting materials the following chemicals were used: LiH (Alfa Aesar, powder, purity 99.4 %), MgB_2 (Sigma-Aldrich, powder, - 100 mesh), titanium (Aldrich, 99.9 %) and TiO_2 (Aldrich, 99.99 %, 21 nm). The as-purchased TiO_2 is composed of a mixture of anatase and rutile phases as the most common and natural form of TiO_2. To quantify the fractions of these phases, an accepted quantitative method and the Rietveld method with the Maud software were used[32-36]. The quantitative method consist in measuring the relative PXD intensities of the anatase [101] *(I_A)* and rutile [110] *(I_R)* peaks (X–Ray cards: Anatase TiO_2: ICSD 93098, Rutile TiO_2: ICSD 93097). The weight fraction of rutile (*X_R*) and anatase (*X_A*) were determined from the following equations:

$$X_R = \frac{1}{1+1.26\left(I_A/I_R\right)} \quad (1)\ [32]$$

$$X_A = 1 - X_R \quad (2)$$

The as-purchased TiO_2 has 0.15-0.17 and 0.83-0.85 of rutile and anatase weight fractions, respectively (ESI: Fig.S1 A and B†). All the materials are designated hereafter as: 2LM (2LiH+MgB_2), 2LM1TiO_2 and 2LM5TiO_2 (2LiH+MgB_2+1 %mol or 5 %mol of TiO_2). Additional reference materials were prepared for XAS measurements at the same milling conditions described above from a stoichiometric mixture of 0.5LiH + TiO_2. After MM the material was composed of Li_xTiO_2 (x = 0.07 and 0.50, ESI: Fig.S2 XRD (a)†). The as-milled 0.5LiH + TiO_2 material was heated up to 400 °C in argon atmosphere resulting in Li_xTiO_2 (x = 0.59 and 1.0, ESI: Fig.S2 XRD (b)†). As purchased Ti–foil and Ti_2O_3 (Sigma Aldrich; 99.9 %) were also used as reference for XAS measurements.

Characterization

Ex-situ Lab powder X-ray diffraction (PXD) experiments (Device: PANalytical Empyrean, CuKa radiation, λ = 1.5405 Å, graphite monochromator, 30 mA and 40 kV) were carried out for crystalline phase identification. A specially sealed chamber was used to avoid the hydrolysis/oxidation during the experiments. *In-situ* PXD with synchrotron radiation (SR–PXD) were preformed in the MAX II Synchrotron in Lund, Sweden, at Beamline I711 in the MAXlab research laboratory using a X–ray wavelength of λ = 0.99917 Å and a Mar 165 CCD detector for data collection[37]. The sample (0.5 mg–2 mg) was airtight encapsulated in a sapphire capillary and then mounted in a specially developed sample holder[38]. The sample holder was connected to the gas system, which was filled with argon and evacuated till vacuum three times before opening the valve to the sample and starting the experiment. Then, the experiment was performed from about 30 °C to 400 °C at a heating rate of 3 °C/min. The SR–PXD data are reported referring to the scattering vector $q = 4\pi \sin\theta/\lambda$ ($Å^{-1}$). FIT2D program was utilized to remove diffraction spots originating from the sapphire tubes and subsequently to transform raw data to powder patterns[39]. The crystallite size of MgB_2 (101) and MgH_2 (110) were determined by the Scherrer equation[40].

Thermogravimetry (TG), Differential scanning calorimetry (DSC) and high pressure-DSC (HP–DSC) measurements were performed with 2LM5TiO_2 sample after the MM and different stages of the hydrogenation and dehydrogenation. TG measurements were performed in a TG device TGA-HP50 – TA Instruments from room temperature to 425 °C – 450 °C at a heating rate of 5 °C/min and under 3 bar of H_2 maintained at a flow of 50 cm^3/min. All samples were put into aluminium capsules in order to minimize the exposure to the air. Then the aluminium capsules were introduced into the TG device in a quartz crucible. HP-DSC measurements were done in a TA-2910 calorimeter from room temperature to 400 °C at a heating rate of 5 °C/min and about 3 bar of H_2. All samples

were put into aluminium capsules, pressed and carried to the HP-DSC device in sealed vessels. Then, the aluminium capsules were introduced into the device exposing them to the air for a short time. For the gas phase analysis of the 2LM5TiO_2 after MM a Hiden HPR-20 QIC device was used.

X-ray Absorption Spectroscopy measurements (XAS) in the XANES region (X-ray absorption near edge structure) for 2LM5TiO_2 samples at different conditions were carried out at at XAFS1 beamline of the National Synchrotron Light Laboratory (LNLS), Campinas, Brazil with ring energy of 1.37 GeV and a ring current of 250 mA[41]. XANES spectra were collected around Ti K-edge (4966 eV) in the energy ranges 4850–5300 eV at ambient temperature. The data were collected in the transmission mode using a Si (111) channel cut monochromator. XAS spectra had their backgrounds corrected by using a polynomial-fit algorithm from the spectral region before the pre-edge. Then the XANES part had the intensity normalized to unity at energy far above the absorption edge (about 5060 eV – 5200 eV) and the spectra were compared with the XANES region of the references. The appropriate amount of material for optimum measurements was calculated by the program "XAFSMASS"[42]. The samples were then mixed with boron nitride (~ 25 mg, Sigma Aldrich, powder, purity: 98 %) in a mortar and pressed into pellets of 7 mm diameter inside a glove box. The pellets were fixed in a circular hole of an aluminium sample holder and sealed with Kapton tape (50 µm in thickness) to prevent the oxidation/hydrolysis of the samples. XAS data processing and fitting were performed by using the "IFEFFIT" software package[43].

High resolution transmission electron microscopy (HR-TEM) images were obtained on a Tecnai G^2 microscope with an information limit of 0.12 nm and Schottky Emission gun operating at 200 kV. 2LM and 2LM5TiO_2 samples were observed at different conditions: after milling, heating, 1st and 10th dehydrogenation, and different stages of the hydrogenation and dehydrogenation at the second cycle. It is important to mention that for each condition of the 2LM5TiO_2 material, each sample was observed at least 5 times and the statistics was done from an average of 50 high resolution images to assure the nanocrystalline structure, nanosize and morphology of the Ti containing phases. Samples for TEM were prepared by dispersing a small amount of powder in hexane and then ultrasonicated 10 minutes before depositing a drop of the resulting suspension on a commercial carbon coated copper grid. The sample was exposed a short time to the air. In order to identify the Ti species rich zone, point elemental analyses *via* energy dispersive X-ray spectroscopy (EDS) were performed – not shown. TEM images processing were done with the following programs: Digital Micrograph (License Nº 90294175), i-TEM (License Nº A2382500) and JEMs (License Nº IEb59yBDflUMh).

For anomalous small-angle X-ray scattering (ASAXS) measurements, samples of 2LM5TiO_2 were prepared after milling, heating, after 1st and 10th cycles. The Ti-ASAXS measurements were performed at the FCM-beamline of the PTB installed at the synchrotron radiation facility BESSY II (HZB, Berlin, Germany)[44]. The beamline was combined with the HZB ASAXS instrument[45]. The four-crystal monochromator[46] has an energy resolution of $\Delta E/E \sim 1x10^{-4}$, while using the Si_{111} crystals. An in vacuum version of a 1M Pilatus detector was used to record the ASAXS data[47]. The advantage of that type of detector is that no window is necessary between the sample and the X-ray detection elements. All measurements were done at two sample-to-detector distances (0.7 m and 3.345 m) to cover the maximum possible experimental q–range. Here, q is the magnitude of the scattering vector: $q = (4\pi/\lambda) \sin\theta$, where λ is the X-ray wavelength and 2θ is the scattering angle. In order to separate the resonant scattering[48] of Ti-containing nanostructures, all measurements were carried out nearby the K absorption-edge of titanium (4966 eV). All selected energies with their corresponding anomalous dispersion factors are listed in Table 1[49].

The samples for ASAXS measurements were mounted on molybdenum sample holder sheets of 0.2 mm thickness with a circular hole of 5 mm in diameter. The samples were supported and sealed within two Kapton tapes from each side of the sample holder, respectively, to avoid any change in oxidation state of the samples.

Raman spectroscopy (RS) measurements were performed on a Confocal Jobin Yvon Micro-Raman T64000 NIR-UV with 20×LWD objective. Spectra of the 2LM and 2LM1TiO_2 materials in dehydrogenated state after 10 absorption–desorption cycles were collected at room temperature with a 514 nm excitation laser and 15 mW of laser power on the sample. The spectra were taken as an average of 10 iterations of 15 seconds. To prevent the samples from air exposure during the RS measurements, the samples (5 mg–10 mg) were loaded into 7 mm diameter aluminium pans and sealed with optical quality glass window inside a glove box. For RS analysis, reference peak positions of $LiBH_4$[50,51], $Li_2B_{12}H_{12}$[52–54], B[53–57] and MgB_2[54,56] were taken from the literature. Spectra for as-purchased MgB_2 (Alfa Aesar, powder, 325 mesh) and $LiBH_4$ (Sigma-Aldrich, purity ≥ 90%) were also collected.

Fourier transformed infrared spectroscopy (FT–IR) measurements of the gas phase for 2LM5TiO_2 were done in a Perkin Elmer–Spectrum 400 device. Gas samples were subtracted each 50 °C during heating from 50 °C to 200 °C. The sample was heated in a sealed vessel connected to a specially designed cell for FT–IR analyses of the gas phase.

Table 1 Selected energies for the ASAXS-measurements at the K-edge of Ti containing compounds and the corresponding anomalous dispersion factors[49]. ΔE [eV] corresponds to the energy used for the measurement minus the energy of the K-edge of Ti.

E_i	Energy [eV]	ΔE [eV]	f'	f''
E_1	4773	-246	-2.801	0.486
E_2	4854	-125	-3.471	0.465
E_3	4931	-48	-4.469	0.455
E_4	4967	-12	-6.058	0.476
E_5	4976	-3	-7.403	0.567

View Article Online
DOI: 10.1039/C7TA03117C

Gas-state FT-IR spectra were obtained from 700 to 4000 cm^{-1}. For FT-IR analysis, reference peak positions of gas diborane were taken from the literature[58]. Moreover, H_2 gas detection analysis (Bacharach combustible gas leak detector) was also performed.

The hydrogen kinetic and thermodynamic properties of the materials were assessed in a Sieverts kind device with mass flow controllers. The hydrogen kinetic behavior of the 2LM, 2LM1TiO_2 and 2LM5TiO_2 was evaluated *via* isothermal hydrogenations and dehydrogenations at 350 °C, 360 °C, 375 °C, 380 °C, 400 °C and 410 °C under 50 bar and 3 bar of hydrogen pressure, respectively. For hydrogenation and dehydrogenation processes the activation energies (Ea) were calculated. The cycling behavior during ten absorption – desorption cycles was measured at 400 °C. The hydrogen gravimetric capacities during cycling were characterized taking into account the error band calculated from the error propagation of the measurement and the device itself[54]. Desorption pressure composition isotherms (PCIs) were measured in the range of temperature between 350 °C and 425 °C for the 2LM5TiO_2 material. The equilibrium plateau pressures were calculated as an average of the experimental points in the plateau region, taking into account the error propagation theory to assign an error range to each calculated equilibrium pressure[59]. From the calculated equilibrium pressures the desorption van't Hoff graph was plotted and the corresponding enthalpy and entropy calculated.

All material handling was carried out in MBraun Unilab glove boxes with oxygen and moisture controlled atmosphere (level of O_2 and H_2O were below 5 ppm, respectively), so as to prevent the oxidation of the samples.

Results and discussion

Characterization of the TiO_2 and Li-RHC interactions

Fig.1 shows *in-situ* SR-PXD during heating, TG and MS results for the as-milled 2LM5TiO_2 material. At the beginning of the *in-situ* SR-PXD, LiH and MgB_2 belonging to the matrix (main phases) are present and remain upon heating. After milling, phases such as $Li_{0.16}TiO_2$ and $Li_{0.5}TiO_2$ are also observed, suggesting that LiH and TiO_2 interacted during milling. In this regard, an analysis of the gas atmosphere of the milling chamber with a Bacharach combustible gas leak detector has confirmed the presence of H_2.

The natural form of TiO_2 is mainly composed of two polymorphs: rutile and anatase. In this work the TiO_2 starting material is a mixture of 0.15-0.17 and 0.83-0.85 of rutile and anatase weight fractions, respectively. TiO_2 rutile is thermodynamically more stable than anatase and its bulk crystalline form can only accommodate a small amount of Li^+ at room temperature[60]. However, TiO_2 anatase is able to uptake lager amounts of Li^+ easily. Thus, it is possible to infer that during milling LiH reacts with TiO_2 polymorphs by forming Li_xTiO_2 (x = 0.16 and 0.50) and releasing H_2 through reaction (1). $Li_{0.16}TiO_2$ is formed from TiO_2 rutile, while Li^+ insertion into TiO_2 anatase brings about $Li_{0.50}TiO_2$, in agreement with previous works[61,62].

$$0.66LiH_{(s)} + 2TiO_{2(s)} \rightarrow Li_{0.16}TiO_{2(s)} + Li_{0.5}TiO_{2(s)} + 0.33H_{2(g)} \quad (1)$$

Upon heating, the *in-situ* SR-PXD (Fig.1 A) exhibits changes regarding the reflections of Li_xTiO_2 phases. TG and MS measurements for 2LM5TiO_2 material also indicate that hydrogen starts being released at about 100 °C (Fig.1 B and C). Although, the MS measurement for the 2LM material does not show any hydrogen release (ESI: Fig.S3†). *In-situ* SR-PXD peak areas and peak positions as a function of the temperature have been analyzed for different reflections belonging to Li_xTiO_2 (x = 0.16, 0.50 and 0.59) (ESI: Fig.S4†). A clear decrease of the $Li_{0.16}TiO_2$ (110) peak area can be observed from about 180 °C till it vanishes at about 360 °C (ESI: Fig.S4 B†). The introduction of Li^+ into the $Li_{0.50}TiO_2$ lattice causes a cell distortion with changes in the cell parameters and an increase of the cell volume, resulting in the $Li_{0.59}TiO_2$ phase formation. Both phases, $Li_{0.50}TiO_2$ and $Li_{0.59}TiO_2$, have the same space group (S.G.) *Imma* and consequently small differences in the peak positions[61]. The peak area and peak position of the $Li_{0.50}TiO_2$ (015) remain almost constant up to 100 °C (ESI: Fig.S4 B and C†). Then, the peak area increases and the peak position noticeably changes to that belonging to $Li_{0.59}TiO_2$ (105) (ESI: Fig.S4 C†). This behavior is consistent with the TG and MS results for 2LM5TiO_2 (Fig. 1 B and C). From about 100 °C to 200 °C, the hydrogen release is fast and then slows down (TG and MS). The diffusion of Li^+ into the lithiated TiO_2 polymorphs lattice is activated by the temperature[62].

Fig. 1 Heating process for 2LM5TiO_2 after milling: **A** *In-situ* SR-PXD; **B** TG and **C**

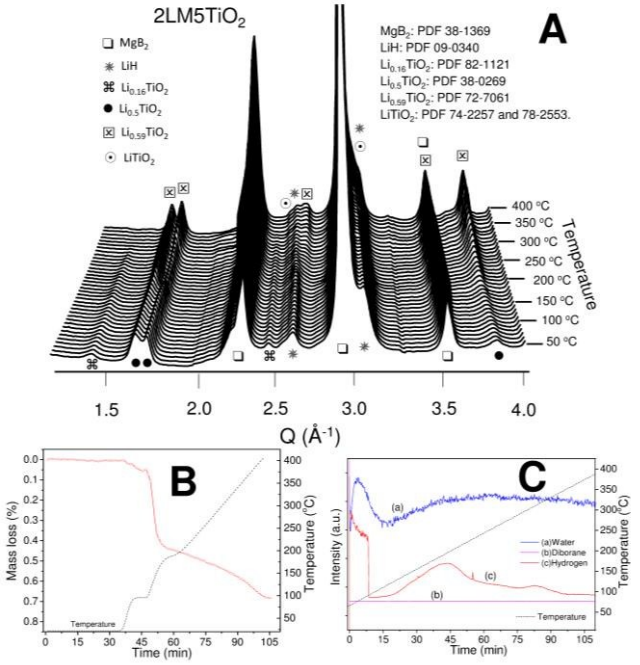

MS.

Therefore, as the temperature goes up, the diffusion of Li^+ accelerates and eventually saturates the present Li_xTiO_2 phases (x = 0.16 and 0.50) *via* the proposed reaction (2). $Li_{0.59}TiO_2$ is clearly detected at 400 °C, while overlapped reflection of $LiTiO_2$ are observed (Q ~ 2.6 $Å^{-1}$ and Q ~ 3.1 $Å^{-1}$; Fig 1 A).

$$0.93LiH_{(s)} + Li_{0.16}TiO_{2(s)} + Li_{0.5}TiO_{2(s)} \rightarrow Li_{0.59}TiO_{2(s)} + LiTiO_{2(s)} + 0.465H_{2(g)} \quad (2)$$

To elucidate the nature and role of Li_xTiO_2 compounds, XANES spectra and HR-TEM images for the $2LM5TiO_2$ material have been performed after milling, heating and hydrogen interaction. The derivatives of the XANES absorption spectra are exhibited in Fig. 2 (ESI: Fig.S5 XANES spectra at Ti edge†).

As noted in the position of the absorption edge of Ti (4975.5 eV) and the shape of the spectrum, the $2LM5TiO_2$ material after milling (Fig.2 (a)) is alike to the one of as-milled $0.5LiH+TiO_2$ (Fig.2 (f)). Thus, LiH reduces TiO_2 from a Ti oxidation state of +4 to near +3. HR-TEM images, fast Fourier transform (FFT) and the respective structure simulations (ESI: Fig. 6S A†) confirm the presence of $Li_{0.16}TiO_2$ and $Li_{0.5}TiO_2$ after milling.

The spectra of the $2LM5TiO_2$ material after heating, 1st dehydrogenation, 2nd hydrogenation and 10th dehydrogenation (Fig.2 (b–e)) exhibit the same position of the absorption edge of Ti (4975 eV) and show similar shapes. It is also noticed that the absorption edge of Ti for $0.5LiH+TiO_2$ after heating (4975 eV; Fig.2 (g)) is slightly lower than that of $2LM5TiO_2$ after milling (4975.5 eV; Fig.2 (a)). It suggests that the same Li_xTiO_2 compounds with higher Li^+ amounts are present after heating and subsequent hydrogen cycling. HR-TEM images and their respective analyses verify the presence of $Li_{0.59}TiO_2$ and $LiTiO_2$ after heating and hydrogen interaction (ESI: Fig. S6 B–E†). These results are in concordance with the *in-situ* SR-PXD, TG and MS outcomes (Fig.1) and the proposed reactions (1) and (2) for the formation of Li_xTiO_2 phases with poor Li^+ amount during milling and subsequent Li^+ saturation after heating and hydrogen interaction, respectively.

For the $2LM5TiO_2$ material after milling, heating, 1st and 10th dehydrogenation, size distributions and morphologies of the Li_xTiO_2 phases have also been investigated *via* ASAXS measurements and HR-TEM observations. Fig.3 shows volume size distributions of the Li_xTiO_2 species derived from ASAXS curves (left) along with their respective HR-TEM images with diffraction patterns (DPs), FFT and simulations (right). The ASAXS scattering curves (ESI: Fig.S7†) exhibit two resonant dispersive features, respectively, at lower *q* value centered at about 0.25 nm^{-1} and a broad hump extended over the *q*-interval of 1.5 nm^{-1}–3 nm^{-1}. The inset plots show with more detail a strong resonant scattering region (0.1 $nm^{-1} < q < 0.6$ nm^{-1}) and a less pronounced resonant scattering region at the higher *q* values within the measurement accuracy. These resonant scattering regions can be attributed to two distinct nanoparticle size distributions in different matrix environments. For this reason, two sets (*j* = 1,2) of

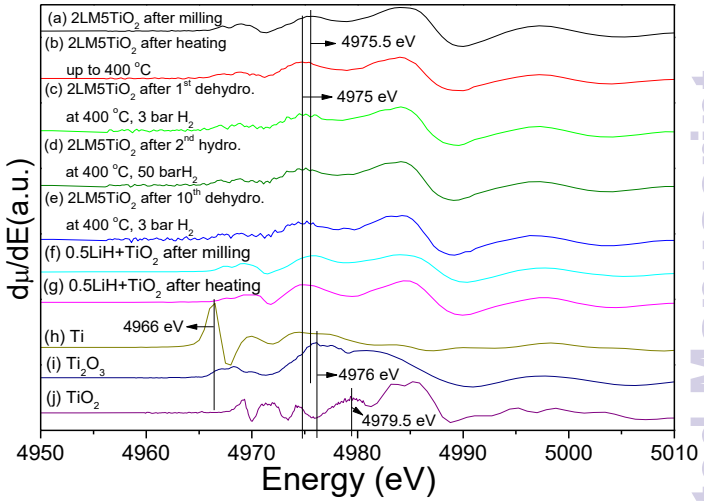

Fig. 2 Derivative of the XANES spectra for 2LM5TiO2 at different stages (a – e) and Reference materials (f – j).

polydisperse spherical containing particles were simultaneously fitted to the ASAXS data measured at four different X-ray energies (E_i; *i*=1, 2, 3, 4; *see* Tabale.1) by the following theoretical intensities[63,64]:

$$I(q,E_i) = \sum_{j=1}^{2} \Delta\rho_j^2(E_i) \int N(r,\sigma_j,R_j) V^2(r) \Psi_j^2(r,q) dr + B(q,E_i) \quad (1)$$

The energy dependent contrast of the j^{th} scattering contribution is represented by $\Delta\rho^2_j(E_i)$. $V(r)$ and $\psi(r,q)$ represent the volume and the form factor of spherical particles, respectively. The latter function is given by the expression:

$$\Psi(r,q) = 3\frac{\sin(qr) - qr\cos(qr)}{(qr)^3} \quad (2)$$

where, q is the scattering vector which is described in the experimental section. $B(q,E_i)$ describes the energy dependent background (fluorescence and resonant-Raman scattering) and the scattering originating from surface roughness and large scale correlations of the powder. To account the polydispersity of Ti containing particles in the hydride matrix,

$$N(r,\sigma_j,R_j) = \frac{1}{\sqrt{2\pi\sigma_j r}} \exp\left[-\frac{\ln\left(r/R_j\right)^2}{2\sigma_j^2}\right] \quad (3)$$

a normalized log-normal distribution was included:

With σ_j being the standard deviation of the distribution and R_j the mean radius parameter of the j^{th} constituent and *r* denote the radius of the spherical particles. For the fitting procedure

View Article Online
DOI: 10.1039/C7TA03117C

of the volume-weighted size distribution (Fig. 3 left) the program SASfit[65] has been used.

After milling the 2LM5TiO_2 material presents $Li_{0.16}TiO_2$ and $Li_{0.5}TiO_2$ nanoparticles with a size distribution in the range of about 10 nm to 30 nm (Fig. 3 A left) consistent with the HR-TEM observations (Fig. 3 A right). On the contrast, after heating, 1st and 10th dehydrogenation the $Li_{0.59}TiO_2$ and $LiTiO_2$ have two nanoparticle size distributions: small particles between ~1 nm and 2 nm and large particles in the range of 5 nm to 30 nm (Fig. 3 B, C, and D, left). According to HR-TEM images, the small particles are only composed of $LiTiO_2$, while the large particles belong to core-shell nanoparticles with a core of $Li_{0.59}TiO_2$ and a shell of $LiTiO_2$ (Fig. 3 B, C and D, right, see ESI: Fig.S8 complete image of core-shell nanoparticles†). Both $LiTiO_2$ and core–shell nanoparticles exhibit rounded shapes in HR-TEM images (Fig. 3 and Fig S8) which validates the assumption of polydisperse spherical containing particles for the ASAXS model (ESI: FigS7† and Fig 3). The detection of Li_xTiO_2 (x= 0.59 and 1) nanoparticles and core-shell particles is in agreement with the work of Borghols *et al.*[66], where titanium oxide polymorphs have been obtained *via* wet-chemistry and the particle size dependence for the Li^+ insertion in TiO_2 has been investigated at room temperature *via* X-ray absorption spectroscopy and *ab-initio* calculations. It has been found that particles of $Li_{0.5}TiO_2$ (s.g. *Imma*) of 7 nm size can be fully saturated to $LiTiO_2$ (s.g.: $I4_1/amd$). For larger sizes, a shell of $LiTiO_2$ of about 4 nm thick covering the $Li_{0.5}TiO_2$ core has formed impeding further Li^+ charging due to the reduced Li^+ uptake diffusion coefficient.

After heating, the core-shell nanoparticles exhibit a shell of $LiTiO_2$ of about 6 nm (Fig.3 B right). However, after the 1st and 10th dehydrogenation the $LiTiO_2$ shells are thinner (about 4 nm) or even disappear and dispersed small $LiTiO_2$ nanoparticles around the $Li_{0.59}TiO_2$ core are observed (Fig.3 C and D, right). This suggests that the $Li_{0.59}TiO_2/LiTiO_2$ ratio changes during hydrogen interaction.

Therefore, samples of 2LM5TiO_2 material have been taken and characterized by HR-TEM (Fig.4 right) at different stages of dynamic hydrogenation and dehydrogenation processes during cycling (Fig.4 left: hydrogen fraction as a function of time). According to PXD analyses for 2LM5TiO_2 at the points indicated in Fig.4 (ESI: Fig. S9†) and previous works[6,8,9], the main phases undergo one step hydrogenation process and two steps dehydrogenation process according to reactions (3), (4) and (5), respectively.

$$\text{Absorption: } 2LiH_{(s)} + MgB_{2(s)} + 4H_{2(g)} \rightarrow 2LiBH_{4(l)} + MgH_{2(s)} \quad (3)$$

$$\text{Desorption: } MgH_{2(s)} \rightarrow Mg_{(s)} + H_{2(g)} \text{ [in liquid } LiBH_4\text{]} \quad (4)$$

$$Mg_{(s)} + 2LiBH_{4(l)} \rightarrow 2LiH_{(s)} + MgB_{2(s)} + 3H_{2(g)} \quad (5)$$

Fig. 3 Characterization of the nanosized particles distribution obtained by ASAXS (left column) and by means of HR-TEM for the Li_xTiO_2 phases in 2LM5TiO_2 material at different stages. General FFT was calculated in each case and compared to simulated ring diffraction patterns (DPs). For core-shell nanoparticles FFT was performed in each region of the particle (core or shell) and compared to Zone Axis DPs in order to establish the phase and orientation of the observed region.

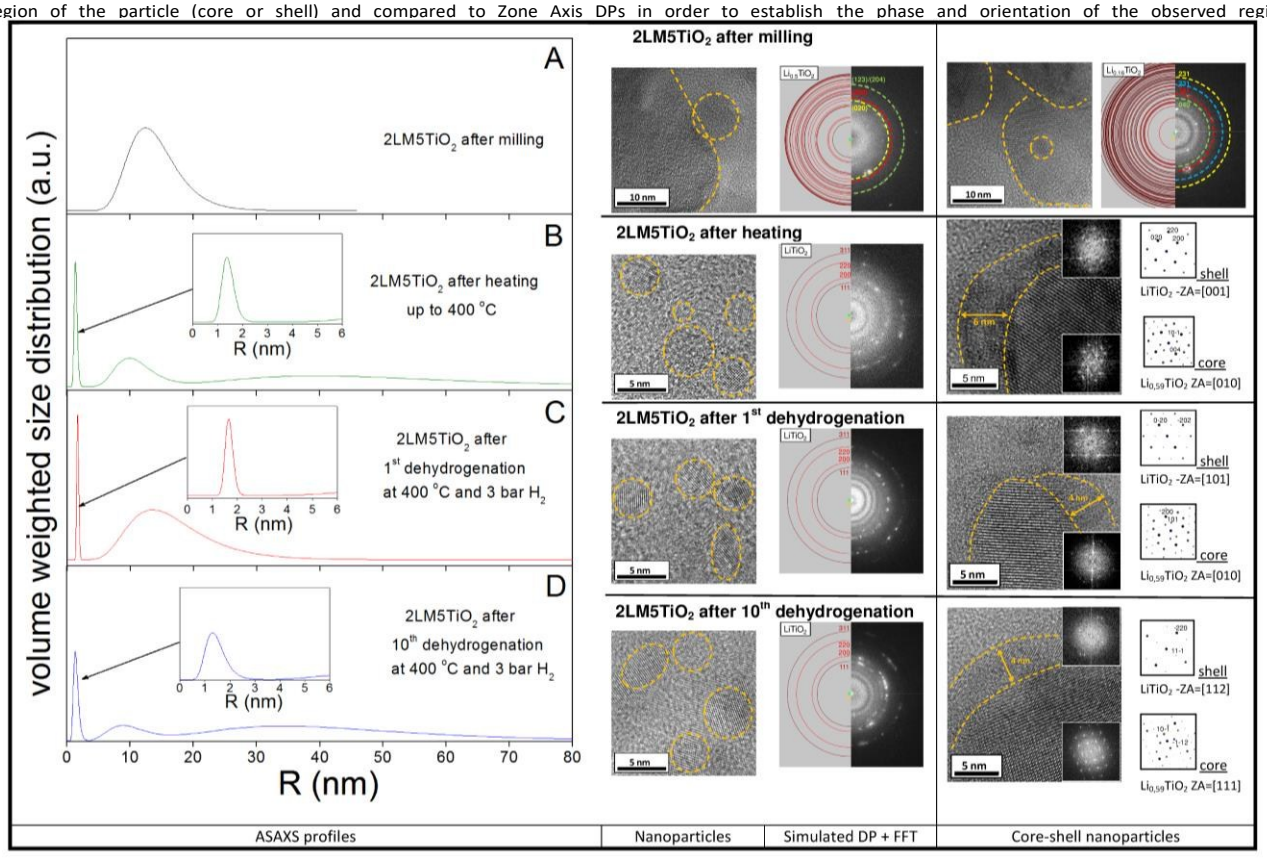

In the case of the additive, the HR-TEM images with their respective FFT and structure simulation (Fig.3 right, ESI: Fig.S10†) show clear changes of the Li_xTiO_2 core–shell nanoparticles. Upon hydrogenation, the thickness of the $LiTiO_2$ shell increases from 1–2 nm (Point 1) to 3–5 nm (Point 2). Upon dehydrogenation, the $LiTiO_2$ shell still grows till about 7 nm during the first step (Point 1). Then, throughout the second step (Point 2 and 3), the $LiTiO_2$ shell decreases up to about 4 nm (Fig.3 and 4 right, ESI: Fig.S10†) and also dispersed small $LiTiO_2$ nanoparticles around the $Li_{0.59}TiO_2$ core are observed (Fig.4 right, ESI: Fig.S10†). These results suggest that $LiBH_4$ interacts with the $Li_{0.59}TiO_2/LiTiO_2$ core–shell nanoparticles. It is important to mention that the differences in the $Li_{0.59}TiO_2/LiTiO_2$ ratio are quite small taking into account that the changes observed *via* HR-TEM are between 3–5 nm. For this reason and owing to the sensitivity of the XANES technique, it is not possible to quantify any difference in the Ti absorption

Fig. 4 Characterization of the nanosized Li_xTiO_2 phases in $2LM5TiO_2$ material during hydrogenation and dehydrogenation by means of HR-TEM. FFT was calculated in each region and compared to simulated diffraction patterns (DPs) in the adequate orientation; the width of the FFT and corresponding simulations is 19.5 nm^{-1}.

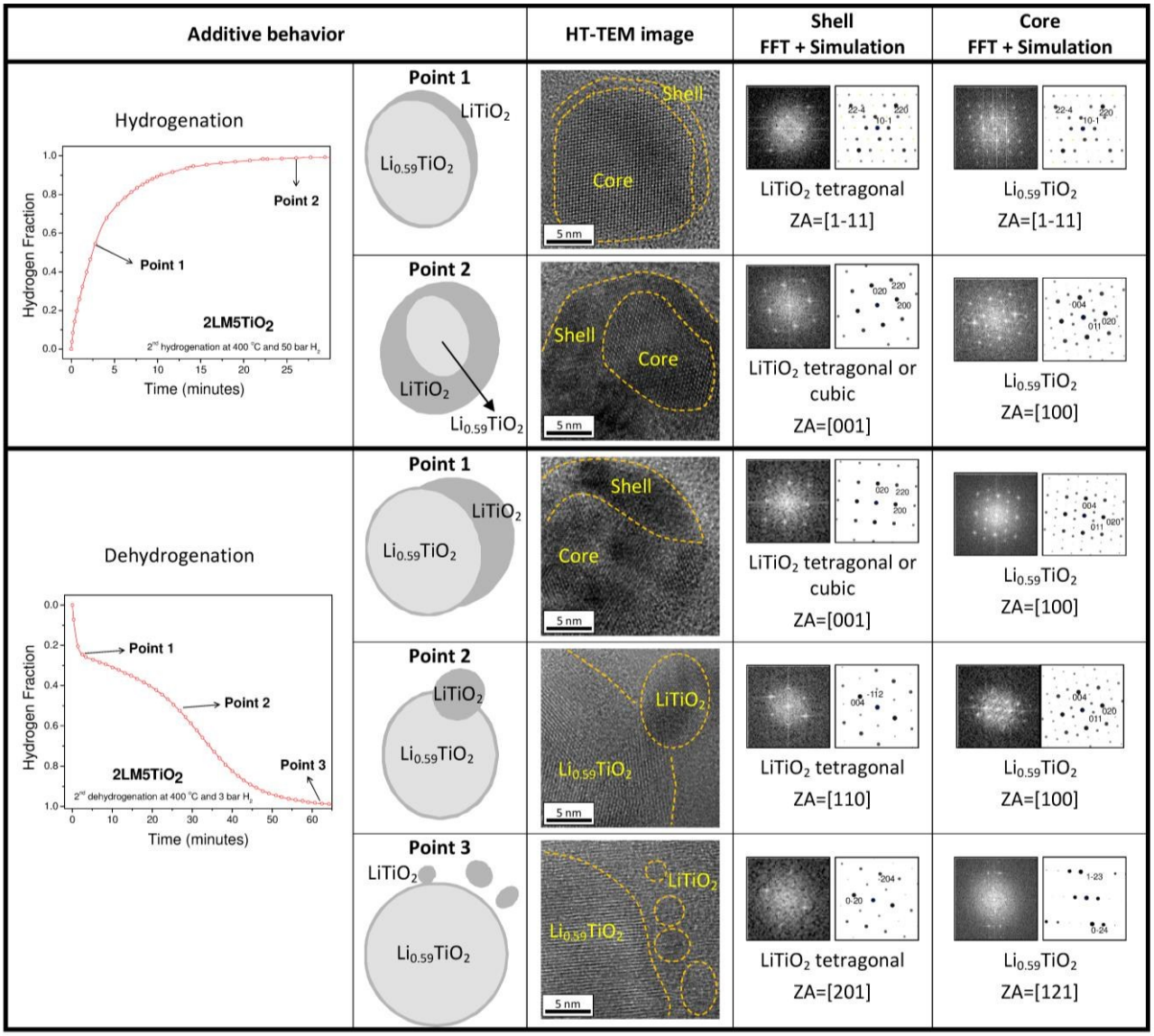

edges between the dehydrogenated (Fig.2 curves (c) and (e)) and hydrogenated (Fig.2 curve (d)) states of the $2LM5TiO_2$ material.

Calorimetric and thermogravimetric analyses (HP-DSC and TG under 3 bar of H_2) of pristine $2LiBH_4+MgH_2$ and samples of $2LM5TiO_2$ taken at point 2 of the dehydrogenation process (Fig.4), show clear evidences of the interactions between $LiBH_4$ and core-shell Li_xTiO_2 nanoparticles (ESI: Fig.S11 – TG and HP-DSC analyses: A and B†). For the above mentioned $2LM5TiO_2$ sample composed of $LiBH_4$, free Mg and Li_xTiO_2 (ESI: Fig.S9 B PXD (b)†) a slight mass loss and the evolution of a broad thermal event start between 90 °C and 140 °C. At about 250 °C the free Mg is re-hydrogenated (EIS: Fig.S11 and Fig.S12 A(b)†) owing to the presence of hydrogen during the non-isothermal measurement. After the melting of $LiBH_4$, the main dehydrogenation process begins at about 300 °C with

View Article Online
DOI: 10.1039/C7TA03117C

the decomposition of MgH_2. Moreover, the $2LM5TiO_2$ sample taken at point 2 of the dehydrogenation process (Fig.4) has been heated up till 200 °C under vacuum and the presence of hydrogen has been verified by Bacharach combustible gas leak detector. FT-IR analyses of the gas phase released from $2LM5TiO_2$ sample taken at point 2 of the dehydrogenation process (Fig.4) have been also performed at 100 °C, 150 °C and 200 °C. There has been no evidence of any boron containing gas species, mainly diborane (ESI: Fig.S12 B†).

These results are in quite agreement with the recent work of Puszkiel *et al.*[67] where it has been found that the presence of core-shell Li_xTiO_2 nanoparticles modify the reaction pathway during the dehydrogenation of $2LiBH_4$-MgH_2 by suppressing the formation of stable $Li_2B_{12}H_{12}$ and noticeably enhance its kinetic behavior. Based on the herein reported experimental evidence, it is possible to infer that the *in-situ* formed core-shell Li_xTiO_2 nanoparticles prompt the early decomposition of $LiBH_4$ *via* a reversible mechanism[62]. During the first step of the dehydrogenation (MgH_2 decomposition: reaction (4), Fig. 4 until Point 1), $LiBH_4$ reacts with $Li_{0.59}TiO_2$ (ESI: Fig.S11 and S12†) by forming a thicker $LiTiO_2$ shell by reaction (6):

$$LiBH_{4(s-l)} + Li_{0.59}TiO_{2(s)} \rightarrow LiTiO_{2(s)} + 0.59LiH_{(s)} + B_{(s)} + 1.705H_{2(g)} \quad (6)$$

Then, the available free Mg and free B coming from the partial decomposition of $LiBH_4$, reaction (6), make possible the beginning of the straight MgB_2 formation acting as trigger of the second step, reaction (5). Bösenberg *et al.*[9] have first reported that the addition of transition metal boride (TM-Borides) such as TiB_2, NbB_2, VB_2 and even additional MgB_2 improves the dehydrogenation behavior of Li-RHC because TM-Borides can provide coherent interfaces to promote the heterogeneous nucleation and growth of MgB_2. Once MgB_2 nuclei are formed, they sustain the further MgB_2 nucleation and growth. As shown in Fig.3 and 4, there is evidence that the $LiTiO_2$ shell is reduced or even disappears after the complete dehydrogenation, suggesting that throughout the further formation of MgB_2, reaction (5), the $LiTiO_2$ shell decomposes according to reaction (7)[67]:

$$LiTiO_{2(s)} + 0.205H_{2(g)} \rightarrow Li_{0.59}TiO_{2(s)} + 0.41LiH_{(s)}. \quad (7)$$

$LiTiO_2$ shell is formed again during hydrogenation process (Fig.4) indicating that the reaction mechanism of Li_xTiO_2 nanoparticles is reversible upon cycling.

Hydrogen storage properties of the Li-RHC+TiO_2

The relevant hydrogen storage properties of Li-RHC with and without TiO_2 are assessed in this section. These properties encompass the dehydrogenation thermodynamics, cycling stability and kinetic behavior: hydrogenation-dehydrogenation kinetic models and activation energies.

Fig.5 shows the equilibrium pressure as a function of the temperature as well as a dehydrogenation PCI at 400 °C (Fig.5 A) and the van't Hoff plot with the calculated dehydrogenation thermodynamic parameters (Fig.5 B) for the $2LM5TiO_2$ material. The dehydrogenation reaction presents two well defined plateaus (Fig.5 A PCI at 400 °C, ESI: Fig.S13 A PCIs†) which account for the reactions steps (4) and (5). The first step, reaction (4), has higher equilibrium pressures (Fig. 5A, PCI and $Peq._4$) and its thermodynamic parameters are ΔH_4= 76±4 kJ/mol H_2 and ΔS_4= 110±10 J/mol K. Both, the equilibrium pressures and the thermodynamic parameters are in agreement with those reported for the dehydrogenation of pure MgH_2[68] and doped MgH_2[69]. PXD results clearly indicate the whole decomposition of MgH_2 after the first step (ESI: Fig.S13 B PXD during the second plateau at 425 °C†). The second plateau (Fig.5 A $Peq._5$ and PCI at 400 °C, ESI: Fig.S13 A second plateau†) belongs to reaction (5) since PXD pattern during the plateau shows the presence of $LiBH_4$, LiH and MgB_2 ascribed to the partial decomposition and formation of these phases, respectively (ESI: Fig.S13 B PXD†). Additionally, at the end of the PCI at 400 °C, the full formation of MgB_2 and LiH is verified by PXD (ESI: Fig.S13 C PXD†). The thermodynamic parameters for the second plateau (reaction (5)) are ΔH_5= 61±4 kJ/mol H_2 and ΔS_5= 107±6 J/mol K in concordance with the literature[27]. Taking into account the obtained thermodynamic parameters, the core-shell Li_xTiO_2 nanoparticles do not have any influence on the thermodynamic behavior of the hydride phases, i.e. reactions (4) and (5).

The PCIs also exhibit a not well-defined third plateau (as indicated in Fig.1 A PCI at 400 °C). Shao *et al.*[27] have investigated the thermodynamic properties of $2LiBH_4$+Ti-catalyzed nanocrystalline MgH_2 and have reported a third plateau attributed to the decomposition of $LiBH_4$ to free B, LiH and H_2 (Fig.5 B, reaction (8)[70]). J. Hu *et al.*[26] have found that the presence of nanoscale MgH_2 suppresses $Li_2B_{12}H_{12}$ formation, hence avoiding the hypothesis that the third plateau corresponds to reaction (9)[71], Fig.5 A.

In our case, the not-well defined third plateau is in the range of 1 to 2.5 bar at 400 °C and at lower temperatures this plateau presents inferior pressure ranges (Fig.5 A PCI and ESI: Fig.S13 A†). The range of pressures of the third plateau is under the desired working backpressure of 3 bar for the dynamic dehydrogenation (Fig.5 A), consequently it does not affect the hydrogen storage properties of interest. Furthermore, the presence of core-shell Li_xTiO_2 nanoparticles precludes the $Li_2B_{12}H_{12}$ formation in spite of the favourable driving force between the $P_{eq.,Li_2B_{12}H_{12}}$ and the 3 bar of H_2 backpressure over 390 °C (Fig.5 A)[67].

View Article Online
DOI: 10.1039/C7TA03117C

Fig. 5 Dehydrogenation thermodynamics of the 2LM5TiO$_2$: **A** Dehydrogenation equilibrium pressures as a function of temperature and dehydrogenation PCI at 400 °C. **B** van't Hoff plot and thermodynamic parameters. Equilibrium pressures and thermodynamic parameters of $LiBH_4$ decomposition reactions[70,71].

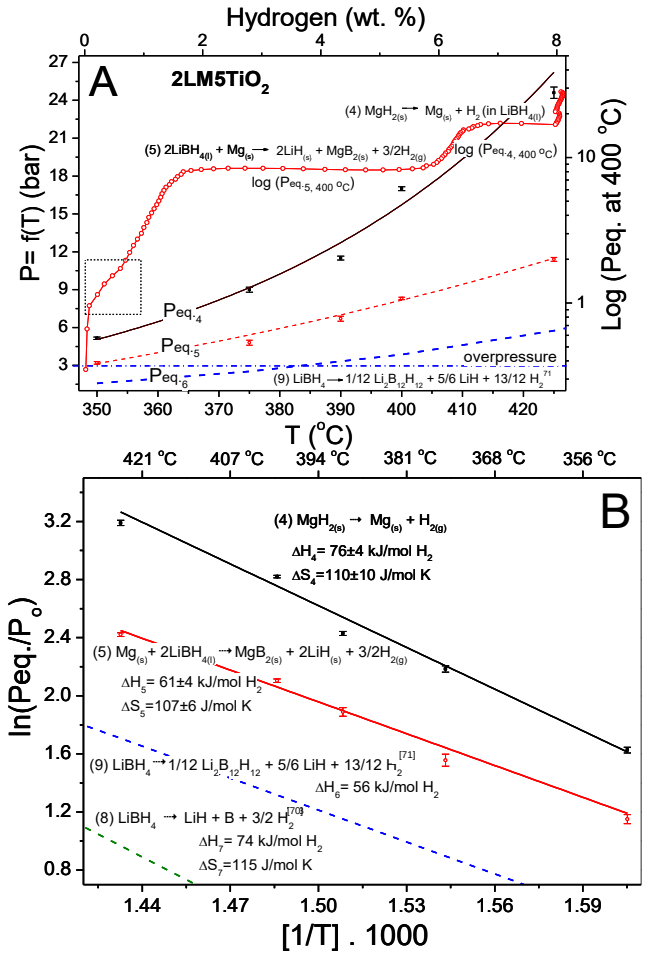

Fig. 6 shows the hydrogen capacity during ten hydrogenation and dehydrogenation cycles for 2LM, 2LM1TiO$_2$ and 2LM5TiO$_2$ at 400 °C under 50 bar and 3 bar of H_2, respectively (ESI: Fig.S14 Kinetic curves†). In the case of 2LM (Fig. 6(a)), the capacity is noticeably lower than the theoretical one (11.4 wt. % H). Adding 5 mol % of TiO_2 sharply reduces the hydrogen capacity owing to the interaction of a relatively large amount of additive with the matrix, *i.e.* Li-RHC (Fig.6 (b)). However, the hydrogen capacity of the 2LM5TiO$_2$ remains stable from the first cycle (6.9±0.3 wt.% H) to the tenth cycle (6.7±0.3 wt.% H). Decreasing the amount of additive up to 1 mol % (2LM1TiO$_2$) results in a markedly increase in the hydrogen capacity to about 10 wt.% and preserves the cycling stability (Fig.6 (c)).

Hydrogenation–dehydrogenation rates for 2LM and 2LM1TiO$_2$ during cycling shown in Fig.7 are expressed as the product of the kinetic constants obtained from fitting kinetic models and the hydrogen gravimetric weight; the error band calculated from the error propagation is also considered. As observed in Fig.7 A, the first hydrogenation is slow and attributed to the stabilization of the materials since they are prepared in dehydrogenated state. Nevertheless, after the first hydrogenation, the 2LM1TiO$_2$ presents noticeably faster hydrogenation and dehydrogenation rates than 2LM (Fig.7 A and B).

PXD and Raman spectroscopy analyses of 2LM and 2LM1TiO$_2$ samples taken after the 10th dehydrogenation evidence the presence of free Mg and amorphous B, $Li_2B_{12}H_{12}$ and remnant $LiBH_4$ for 2LM, while 2LM1TiO$_2$ only shows MgB_2, LiH and the additive, which demonstrates full reversibility of the hydride system (Fig.S15 A PXD and B Raman spectra†). After cycling MgB_2, phase responsible for the reversibility of the hydride system[2,3], has a reduced grain size of 10 nm for the 2LM1TiO$_2$ in comparison with 30 nm for the 2LM.

These results reveal that the presence of a small amount of *in-situ* formed core-shell Li_xTiO_2 nanoparticles leads to a clear enhancement of the hydrogen capacity, cycling stability (Fig.6) and hydrogenation-dehydrogenation rates (Fig.7) of

Fig. 6 Hydrogen capacity during cycling calculated from the dehydrogenation kinetic curves: (a) and (b) 2LM, (c) and (d) 2LM1TiO$_2$ and (e) and (f) 2LM5TiO$_2$. Absorption and desorption at 400 °C under 50 bar H_2 and 3 bar H_2, respectively.

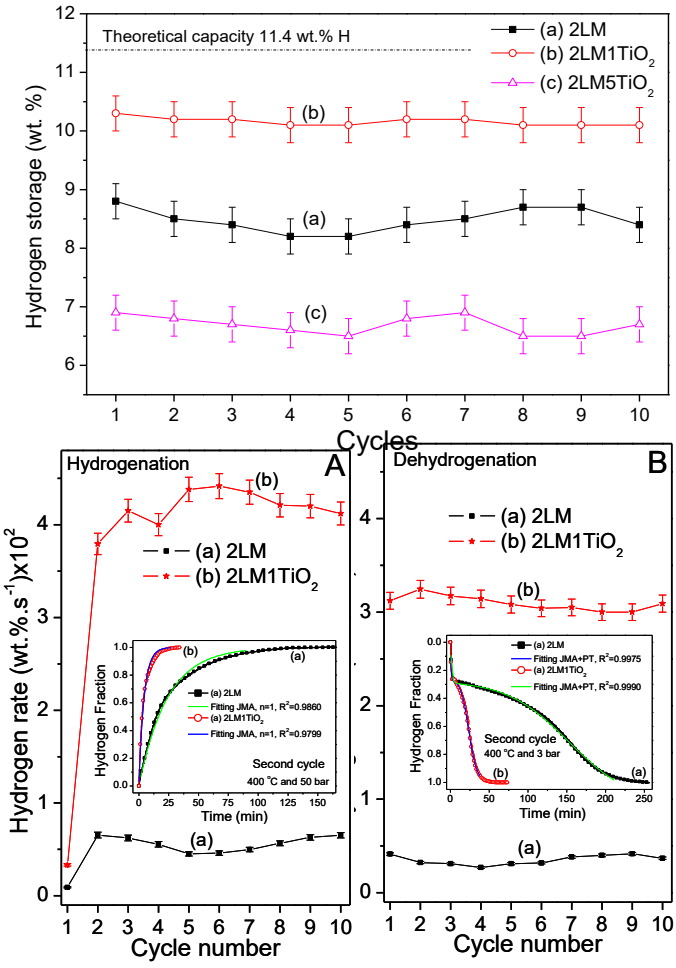

Fig. 7 A Hydrogenation rates under 50 bar H_2 **B** dehydrogenation rates of the second step under 3 bar H_2 during cycling at 400 °C for 2LM and 2LM1TiO$_2$. Inset plots: Hydrogen kinetic curves of the 2nd cycle and model fitting: the models are fitted between 0.10 – 0.90 of the hydrogen fraction.

the Li-RHC. These improvements account for the reversible Li^+ sink/source effect facilitating the direct reaction of $LiBH_4$ with Mg to form LiH, MgB_2 under low overpressure[62], the prevention of the material's agglomeration and improved microstructural refinement of MgB_2 conferred by the presence of the Li_xTiO_2 nanoparticles.

In the inset plots of Fig.7 the kinetic curves of the second hydrogenation and dehydrogenation as well as the kinetic models fitted curve for 2LM and 2LM1TiO_2 are also exhibited. The Sharp's[72] and Jone's[73] method was applied to identify the proper rate limiting step mechanism for the hydrogenation process: plotting the experimental value of $(t/t_{0.5})_{experimental}$ versus the theoretical ones $(t/t_{0.5})_{theoretical}$. For all hydrogenation cycles at 400 °C and even lower temperatures, the Johnson-Mehl-Avrami (JMA) reaction model with n= 1 (one dimensional interface-controlled reaction) is the most suitable one in agreement with previous works[9,10] (ESI: Fig.S16†). The JMA gas–solid reaction model is based on nucleation and growth of transformations in metals and alloys[74]. This model describes the reaction in terms of the following equation (4):

$$f = 1 - \exp\left[-(k.t)^n\right] \qquad (4)$$

where, f is the transformed fraction, k the rate constant, t is time and n is the so-called Avrami exponent which is related to the dimensionality of the growth process (1, 2 and 3 for 1D, 2D and 3D growth, respectively) and provides information about the rate limiting step of the reaction (interface controlled growth= 1 and diffusion controlled growth= 2). All the hydrogenation curves present good fitting agreements with correlation coefficient R^2 near 1 (ESI: Table S1 JMA fitting parameters for all the hydrogenation curves†). The hydrogen uptake proceeds in a single-step mechanism as described in reaction (3). Fig.8 A shows the hydrogenation activation energies (Ea) of this single step reaction for 2LM and 2LM1TiO_2 (kinetic curves fitting ESI: Fig.S17 A and B†). As noticed, both Ea values are identical (2LM= 91±1 kJ/mol H_2 and 2LM1TiO_2= 91±3 kJ/mol H_2), though the pre-exponential factor (A) for 2LM1TiO_2 is about five times larger (2LM= $7.7x10^3$ and 2LM1TiO_2= $3.9x10^4$). The markedly improvement in the hydrogenation kinetic behavior (Fig.7 A) can be ascribed to two main factors: microstructure of the MgB_2 and the effect of the additive. Thus, the reduced size of MgB_2 in 2LMTiO_2 and the increased pre-exponential factor (A) related to the high Li^+ mobility through the Li_xTiO_2 lattice [60,64] accelerate the one dimensional interface-controlled mechanism during hydrogenation.

The dehydrogenation kinetic curves for Li-RHC with and without TiO_2 during cycling at 400 °C (Fig.7 B) and all the tested range of temperature (from 380 °C to 410 °C and under 3 bar of H_2) are fitted by a novel proposed approach by the combination of two kinetic models: JMA[74] for the first step (reaction (4)) and modified Prout-Topkins[75] (PT) for the second step (reaction (5)) from 0.10 to 0.95 of the hydrogen fraction. The JMA gas-solid model with n= 1 is suitable for the first step. As the second step involves a gas-solid-liquid reaction, the modified autocatalytic PT model has been successfully used to model solid-fluid and gas-solid-liquid reactions[75,76] such as a gas-solid-liquid reaction among $Al_{(s)}$, $LiBH_{4(l)}$ and $H_{2(g)}$[77]. Consequently, this novel approach can be described by the following equation (5):

$$f = A_1\underbrace{\left(1-\exp\left[-(k_1.t)^n\right]\right)}_{JMA} + A_2\underbrace{\left(1+\exp\left[-(k_2.(t-t_0))^m\right]\right)}_{PT} \qquad (5)$$

Here f is the transformed fraction, k_1 and k_2 the rate constants for the first and second steps, respectively, t is time, t_0 is the time at f= 0.5, n= 1, m is the PT model exponent that is equal to – 1 and A_1 and A_2 are fitting factors. The fitting of equation (5) to the dehydrogenation curves during cycling (Fig.7 B) presents good agreement with correlation coefficient R^2 near one (ESI: Table S2 JMA+PT fitting parameters†).

The decomposition of MgH_2 during the first step for 2LM and 2LM1TiO_2 is limited by a MgH_2/Mg interface-controlled mechanism along one-dimensional dislocation lines (JMA, n≈ 1)[78,79]. Fig.8 B exhibits the dehydrogenation Ea for 2LM and 2LM1TiO_2 corresponding to the first and second steps (kinetic curves fitting ESI: Fig.S18 A and B†). For the MgH_2 desorption, the Ea lowers from 137±6 kJ/mol H_2 for 2LM to 123±7 kJ/mol H_2 for 2LM1TiO_2. The grain sizes of MgH_2 for hydrogenated 2LM and 2LM1TiO_2 after cycling are 20 nm and 8 nm, respectively (ESI: Fig.S19 PXD†).

These results suggests that the reaction kinetics of the first step of the dehydrogenation process for 2LM1TiO_2 is enhanced by the decreased grain size of MgH_2 and the well-known catalytic effect of transition metals oxides on the kinetic behavior of MgH_2[80].

Fig.8 B (b) and (d) show the dehydrogenation Ea belonging to the second step for 2LM and 2LM1TiO_2, respectively. As seen, the dehydrogenation Ea for 2LM1TiO_2 (241±4 kJ/mol H_2) is lower than that for 2LM (256±7 kJ/mol H_2). This is in

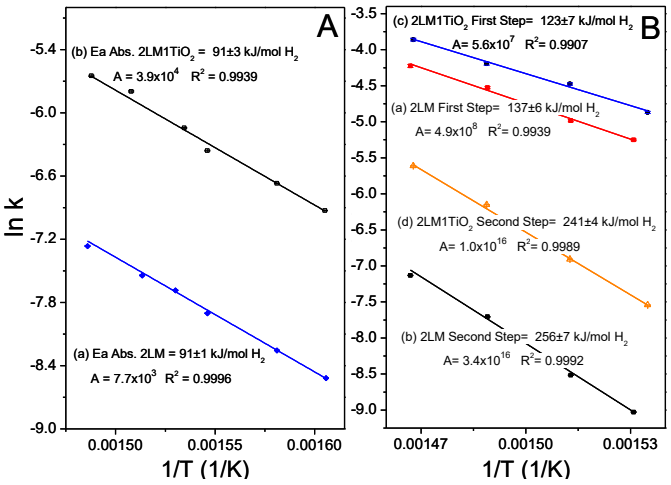

Fig.8 A Hydrogenation and **B** Dehydrogenation activation energy plots for 2LM and 2LM1TiO_2.

agreement with the fitted modified autocatalytic PT model, which takes into account the involvement of the products as reactive phases[70]. Herein, the autocatalysis is interpreted in terms of enhanced nucleation and growth of MgB_2 promoted by the early formed MgB_2 nuclei. In this regard, the *in-situ* formed core-shell Li_xTiO_2 nanoparticles catalyses the second step of the dehydrogenation of Li-RHC, acting as a Li^+ source according to the described mechanism (reaction (6) and (7))[67] and further enhancing the heterogeneous nucleation and growth of MgB_2.

Conclusions

Detailed investigations of the effects of *in-situ* formed core-shell Li_xTiO_2 nanoparticles on the hydrogen storage properties of $2LiH+MgB_2/2LiBH_4+MgH_2$ material (Li-RHC) have shown noticeably improvements in terms of kinetic behavior, hydrogen capacity and cycling stability. In comparison with the pristine Li-RHC, the 1 mol % TiO_2 doped Li-RHC has an increased hydrogen storage capacity of about 10 wt.%, noticeably reduced hydrogenation and dehydrogenation times of 25 minutes and 50 minutes at 400 °C, respectively, and sustainable cycling stability. The presence of *in-situ* formed core-shell Li_xTiO_2 nanoparticles does not modify the dehydrogenation thermodynamic properties of the Li-RHC itself, but it confers proper microstructural refinement to the Li-RHC with reduced MgH_2 and MgB_2 grain sizes preventing the material's agglomeration upon cycling, increases the Li^+ mobility and reduces the dehydrogenation Ea during the whole dehydrogenation process. These improvements are due to the catalytic mechanism of the *in-situ* formed core-shell Li_xTiO_2 nanoparticles *via* a reversible Li^+ source/sink reaction upon hydrogenation and dehydrogenation. This research proposes a new and attractive way to improve the kinetic behavior of Li-multi-component hydrogen storage systems using low-cost additives such as TiO_2.

Acknowledgements

The authors thank CONICET (Consejo Nacional de Invetigaciones Científicas y Técnicas), ANPCyT – (Agencia Nacional de Promoción Científica y Tecnológica), CNEA (Comisión Nacional de Energía Atómica), HZG (Helmholtz–Zentrum Geesthacht), PTB (German National Metrology Institute) FCM-Beamline, Michael Krumrey, HZB-BESSY II Laboratory (Proposal ID: 14100931), Lund University–MAX IV Laboratory – Beamline I711: *in-situ* XRD measurements (Proposal ID: 20140433) and Laboratorio Nacional de Luz Sincrotron (LNLS), Campinas, Brazil (Proposal XAFS1-15239) for financial support to carry out this work. We would also like to thank the Metals Physics Division for the TEM devices, the Characterization Material Division for the XRD apparatus, Low Temperature Division for the Raman device, Sebastian Anguiano for the needful assistance to perform the Raman measurements and Eike Gericke from HZB for the assistance with the ASAXS measurements. The researchers leading to these results have received funding from the European Marie Curie Actions under ECOSTORE grant agreement no. 607040.

References

1 M. Felderhoff, C. Weidenthaler, R. von Helmolt and U. Eberle, *Phys. Chem. Chem. Phys.*, 2007, **9**, 2643.
2 G. Barkhordarian, T. Klassen, M. Dornheim and R. Bormann, *J Alloy Compd.*, 2007, **440**, L18.
3 J.J. Vajo, S.L. Skeith and F. Mertens, *J.Phys. Chem. B*, 2005, **109**, 3719.
4 J. Jepsen, C. Milanese, A. Girella, G.A. Lozano, C. Pistidda and J.M. Bellosta von Colbe, *et al.*, *Int. J. Hydrogen Energy*, 2013, **38**, 8357.
5 J. Jepsen, J.M. Bellosta von Colbe, T. Klassen and M. Dornheim, *Int. J. Hydrogen Energy*,2012, **37**, 4204.
6 U. Bösenberg, S. Doppiu, L. Mosegaard, G. Barkohrdarian, N.eigen and A. Borgschulte, *et al.*, *Acta Mater.*, 2007, **55**, 3951.
7 F. E. Pinkerton, M. S. Meyer, G. P. Meisner, M. P. Balogh and J. J. Vajo, *J. Phys. Chem. C*, 2007, **111**, 12881.
8 U. Bösenberg, D. B. Ravnsbæk, H. Hagemann, V. D'Anna, C. Bonatto Minella and C. Pistidda, *et al.*, *J. Phys. Chem. C*, 2010, **114**, 15212.
9 U. Bösenberg, J.W. Kim, D. Gosslar, N. Eigen, T.R. Jensen and J.M. Bellosta von Colbe, *et al.*, *Acta Mater.*, 2010, **58**, 3381.
10 J.A. Puszkiel, F.C. Gennari, P. Arneodo Larochette, J.M. Ramallo-López, U. Vainio and F. Karimi, *et al.*, *J. of Power Sources*, 2015, **284**, 606.
11 T. Sun, H. Wang, Q. G. Zhang, D. L. Sun, X. D. Yao and M. Zhu, *J. Mater. Chem.*, 2011, **21**, 9179.
12 J. F. Mao, Z. P. Guo, X. B. Yu and H. K. Liu, *J. Mater. Res.*, 2011, **26**, 1143.
13 E. Deprez, A. Justo, T. C. Rojas, C. Lopez-Cartes, C. B. Minella and U. Bösenberg, *et al.*, *Acta Mater.*, 2010, **58**, 5683.
14 H. Q. Kou, X. Z. Xiao, J. X. Li, S. Q. Li, H. W. Ge and Q. D. Wang, *et al.*, *Int. J. Hydrogen Energy*, 2012, **37**, 1021–1026.
15 X. Z. Xiao, J. Shao, L. X. Chen, H. Q. Kou, X. L. Fan and S. S. Deng, *et al.*, *Int. J. Hydrogen Energy*, 2012, **37**, 13147.
16 X. Kang, K. Wang, Y. Zhong, B. Yang and P. Wang, *J. Mater. Chem. A*, 2013, **15**, 2153.
17 J. Shao, X. Xiao, L. Chen, X. Fan, L. Han and S. Li, *et al.*, *J. Mater. Chem. A*, 2013, **1**, 10184.
18 X. Fan, X. Xiao, L. Chen, X. Wang, S. Li and H. Ge, *et al.*, *J. Mater. Chem. A*, 2013, **1**, 11368.
19 K. Wang, X. Kang, Q. Kang, Y. Zhong, C. Hud and P. Wang, *J. Mater. Chem. A*, 2014, **2**, 2146.
20 T.K. Nielsen, U. Bösenberg, R. Gosalawit, M. Dornheim, Y. Cerenius and F. Besenbacher, *et al.*, *ACS Nano*, 2010, **4**, 3903.
21 R. Gosalawit-Utke, T.K. Nielsen, I. Saldan, D. Laipple, Y. Cerenius and T.R. Jensen, *et al.*, *J. Phys. Chem. C*, 2011, **115**, 10903.
22 R. Gosalawit-Utke, T.K. Nielsen, K. Pranzas, I. Saldan, C. Pistidda and F. Karimi, *et al.*, *J. Phys. Chem. C*, 2012, **116**, 1526.
23 R. Gosalawit-Utke, C. Milanese, T.K. Nielsen, F. Karimi, I. Saldan and K. Pranzas, *et al.*, *Int. J. Hydrogen Energy*, 2013, **38**, 1932.
24 R. Gosalawit-Utke, C. Milanese, P. Javadian, J. Jepsen, D. Laipple and F. Karimi, *et al.*, *Int. J. Hydrogen Energy*, 2013, **38** 3275.
25 R. Gosalawit-Utke, C. Milanese, P. Javadian, A. Girella, D. Laipple and J. Puszkiel, *et al.*, *J Alloy Compd.*, 2014, **599**, 78.
26 J.Hu, R. Witter, H.Shao, M. Felderhoff and M. Fichtner, *J. Mater. Chem. A*, 2014, **2**, 66.

27 H.Shao, M.Felderhoff and C. Weidenhalter, *J. Phys. Chem. C*, 2015, **119**. 2341.
28 Y. Zhong, X. Wan, Z. Ding and L. L. Shaw, *Int. J. Hydrogen Energy*, 2016, **41**, 22104.
29 G. Xia, Y. Tan, F. Wu, F. Fang, D. Sun and Z. Guo, *et al.*, *Nano Energy*, 2016, **26**, 488.
30 M. Paskevicius, L. H. Jepsen, P. Schouwink, R. Černy, D. B. Ravnsbæk, Y. Filinchuk, *et al.*, *Chem. Soc. Rev.*, 2017, **46**, 1565.
31 X. Yu, Z. Tang, D. Sun, L. Ouyang, M. Zhu, *Progress in Materials Science*, 2017, **88**, 1.
32 R. A. Spurr and H. Myers, *Anal. Chem.*, 1957, **29,** 760.
33 H. M. Rietveld, *Acta Crystallogr.*, 1967, **22**, 151.
34 H. M. Rietveld, *J. Appl. Crystallogr.*, 1969, **2**, 65.
35 L. Lutterotti, S. Matthies, H. R. Wenk, A. S. Schultz and J. W. Richardson, *J. Appl. Phys.*, 1997, **81**, 594.
36 H. R. Wenk, L. Lutterotti and S. C. Vogel, *Powder Diffr.*, 2010, **25**, 283.
37 Y. Cerenius, K. Staal; L.A. Svensson, T. Usby, A. Oskasson and J. Albertson, *et al.*, *J. Synchrotron Rad.*, 2000, **7**, 1.
38 T.R. Jensen, T.K. Nielsen, Y. Filinchuck, J.E. Jørgensen, Y. Cerenius and M.E. Gray, *et al.*, *J. Appl. Cryst.*, 2010, **43**, 1456.
39 A. P. Hammersley, FIT2D: An Introduction and Overview, ESRF Internal Report, ESRF97HA02T, FIT2D: An Introduction and Overview, 1997.
40 L. Alexander, P.H. Klug, *J. Appl. Phys.*, 1950, **21**, 137.
41 Laboratorio Nacional de Luz Síncrotron (LNLS). http://www.lnls.br 28. Accessed August 2004
42 K. V. Klementiev, XAFSmass, freeware: www.cells.es/Beamlines/CLAESS/software/xafsmass.html.
43 B. Ravel and M. Newville, *J. Synchrotron Rad.*, 2005, **12 (4)**, 537.
44 M. Krumrey, *J. Synchrotron Rad.*, 1998, **5**, 6.
45 H. Bieder, A. Hoell, L. Mokrani and I. Zizak, Patent **DE102006029449**. 2007.
46 M. Krumrey, G. Ulm, *Nucl. Instr. and Meth. A*, 2001, **467–468**, 1175.
47 J. Wernecke, C. Gollwitzer, P. Müller and M. Krumrey, *J. Synch. Rad.,* 2014, **21**, 529.
48 A. Hoell, D. Tatchev, S. Haas, J. Haug and P. Boesecke, *J. Appl. Cryst.,* 2009, **42**, 323.
49 D. T. Cromer, *J. Chem. Phys.*, 1970, **53**, 1891.
50 Orimo, Y. Nakamori and A. Züttel, *Mater. Sci. Eng. B*, 2004, **108**, 51.
51 Y. Yan; A. Remhof, S. J. Hwang, H.W. Li, P. Mauron and S. Orimo, *et al.*, *Phys. Chem. Chem. Phys.*, 2012, **14**, 6514.
52 Y. Yan, H.-W. Li, H. Maekawa, K. Miwa, S. Towata and S. Orimo, *J. Phys. Chem. C*, 2011, **115**, 19419.
53 J.-H. Shim, J.-H. Lim, S.-U. Rather, Y.-S. Lee, D. Reed and Y. Kim, *et al.*, Y. *J. Phys. Chem. Lett.*, 2010, **1**, 59.
54 K.-B. Kim, J.-H. Shim, S.-H. Park, I.-S. Choi, K. H. Oh and Y. W. Cho, *J. Phys. Chem. C*, 2015, **119**, 9714.
55 S.-I Orimo, Y. Nakamori, N. Ohba, K. Miwa, M. Aoki, S.-I. Towata and A. Züttel, *Appl. Phys. Lett.*, 2006, **89**, 1.
56 J. Purewal, S.-J. Hwang, R. C. Jr. Bowman, E. Rönnebro, B. Fultz and C. Ahn, *J. Phys. Chem. C.*, 2008, **112**, 8481.
57 Z.G. Zhang, F.P. Luo, H. Wang, J.W. Liu and M. Zhu, *Int. J. of Hydrgen Energy*, 2012, **37**, 926.
58 R.C. Lord, E. Nielsen, *J. Chem. Phys.*, 1951, **19**, 1
59 J.A. Puszkiel, PhD Thesis, Universidad Nacional de Cuyo, Instituto Balseiro, 2012. http://ricabib.cab.cnea.gov.ar/328/.
60 S. Takai, M. Kamata, S. Fujine, K. Yoneda and K. Kanada, *Solid State Ion*, 1999, **123**, 165.
61 J. Akimoto, Y. Gotoh, Y. Oosawa, N.Nonose, T. Kumagai and K. Aoki, *J. Solid State Chem.*, 1994, **113**, 27.
62 M. Wagemaker, G. J. Kearley, A. A. Van Well, H. Mutka and F. M. Mulder, *J. Am. Chem. Soc.,* 2003, **125***,* 840.
63 A. Henningsson, H. Rensmo, A. Sandell, H. Siegbahn, S. Sodergren and H. Lindstrom, *et al.*, *J. Chem. Phys.*, 2003, **118**, 5607.
64 A. Stashans, S. Lunell, R. Begstrom, A. Hagfedt and S.E. Lindquist, *Phys. Rev. B*, 1996, **53**, 159.
65 I. Breβler, J. Kohlbrecher and A.F. Thünemann, *J Appl Crystallogr.*, 2015, **48**, 1587.
66 W. J. H. Borghols, D. Lützenkirchen-Hecht, U. Haake, E. R. H. van Eck, F. M. Mulder and M. Wagemaker, *Phys. Chem. Chem. Phys*., 2009, **11**, 5742.
67 J. Puszkiel, M.V. Castro Riglos, F. Karimi, A. Santoru, C. Pistidda and T. Klassen, *et al.*, *Phys. Chem. Chem. Phys.*, 2017, **19**, 7455.
68 J.F. Jr. Stampfer, C.E. Jr. Holley and J.F. Suttle,. *J Am. Chem. Soc.,* 1959, **82**, 3504.
69 J.A. Puszkiel, P. Arneodo Larochette and F.C. Gennari, *J. of Power Sources,* 2009, **186**, 185.
70 *P. Mauron, F. Buchter, O.Friedrichs, A. Remhof, M. Bielmann and C. N. Zwicky, et al., J. Phys. Chem. B,* 2008, **112**, 906.
71 K. Miwa, N. Ohba, S. I. Towata, Y. Nakamori and S. I. Orimo, *Phys. Rev. B*, 2004, **69**, 245120.
72 J. H. Sharp, and G.W. Brindley, B.N. Achar, *J. Am. Ceram. Soc.*, 1966, **49**, 379.
73 L.F. Jones, D. Dollimore and T. Nicklim, *Thermochim. Acta* 1975, **13**, 240.
74 J.W. Christian, The theory of transformations in metals and alloys. 3rd ed. Amsterdam: Pergamon; 2002.
75 M.E. Brown, *Thermochim. Acta*, 1997, **300**, 93.
76 S.B. Jagtap, B.B. Kale and A.N. Gokarn, *Metall. Mater. Trans. B*, 1992, **67**, 45.
77 Y. Zhang, Q. Tian, J. Zhang, S.S. Liu and L.-X. Sun, *J. Phys. Chem. C*, 2009, **113**, 18424.
78 Y. Wang, C. An, Y. Wang, Y. Huang, C. Chen and L. Jiao, *et al.*, J. *Mater. Chem. A*, 2014, **2**, 16285.
79 K.-J. Jeon, H. R. Moon, A. M. Ruminski, B. Jiang, C. Kisielowski and R. Bardhan, *et al.*, *Nature mater.*, 2011, **10**, 286.
80 G. Barkhordarian, T. Klassen and R. Bormann, *J. Phys. Chem. B*, 2006, **110**, 11020.

View Article Online
DOI: 10.1039/C7TA03117C

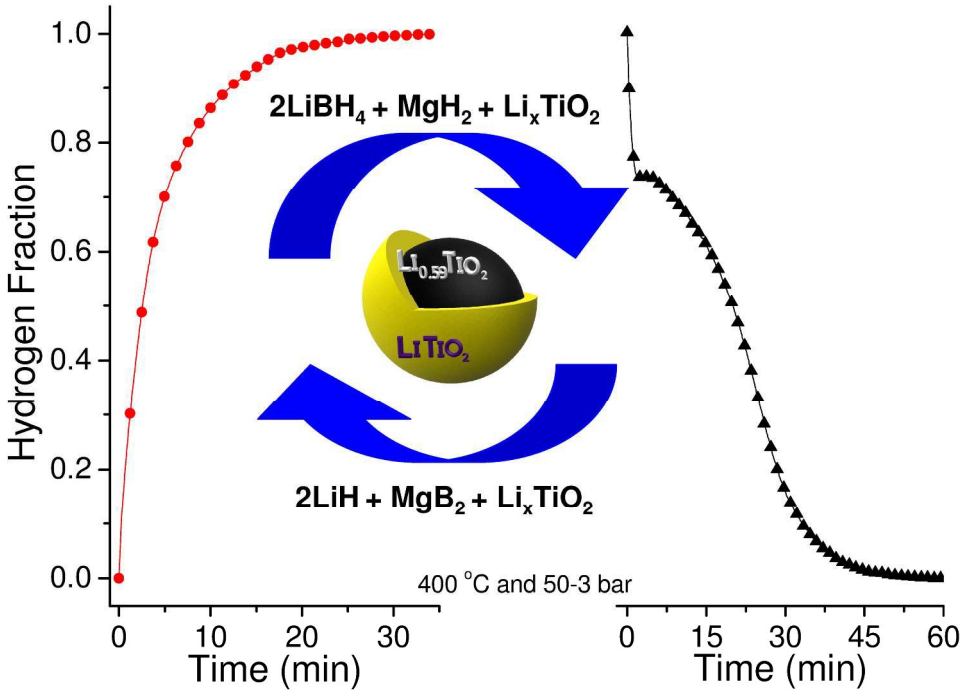

131x97mm (600 x 600 DPI)